Guiding of visible photons at the ångström thickness limit

Xingwang Zhang¹, Chawina De-Eknamkul¹, Jie Gu², Alexandra L. Boehmke¹, Vinod M. Menon¹, Jacob Khurgin³ and Ertugrul Cubukcu¹, Alexandra L. Boehmke¹, Vinod M. Menon¹,

Optical waveguides are vital components of data communication system technologies, but their scaling down to the nanoscale has remained challenging despite advances in nano-optics and nanomaterials. Recently, we theoretically predicted that the ultimate limit of visible photon guiding can be achieved in monolayer-thick transition metal dichalcogenides. Here, we present an experimental demonstration of light guiding in an atomically thick tungsten disulfide membrane patterned as a photonic crystal structure. In this scheme, two-dimensional tungsten disulfide excitonic photoluminescence couples into quasi-guided photonic crystal modes known as resonant-type Wood's anomalies. These modes propagate via total internal reflection with only a small portion of the light diffracted to the far field. Such light guiding at the ultimate limit provides more possibilities to miniaturize optoelectronic devices and to test fundamental physical concepts.

tomically thin transition metal dichalcogenides (TMDCs) are two-dimensional (2D) direct bandgap semiconductors with unique optical properties^{1,2}. They have been studied in great detail for their potential in nanophotonic applications^{3,4} thanks to their photoluminescence (PL) emission^{5–7} and optical non-linearity^{8–10}. TMDCs have been integrated onto optically resonant structures made of conventional bulk materials to make nanophotonic devices^{4,11,12}. However, the utility of atomically thick TMDC semiconductors themselves as independent nanophotonic functional elements remains to be demonstrated. To this end, the simplest photonic component that involves moulding the propagation of visible light in such atomically thick materials is an optical waveguide based on total internal reflection.

Recently, our theoretical investigation showed that single-mode waveguiding of visible light is possible in a subnanometre-thick TMDC layer¹³. This elusive transverse electric (TE) polarized waveguide mode exists at the ångström thickness limit strictly for a symmetric environment (Supplementary Sections 1 and 2). Furthermore, the supported waveguide mode with an effective mode index of near unity¹³ is bound to the TMDC layer, which prohibits far-field probing.

Here we show that TMDC photonic crystals (PhCs) can overcome the fundamental light-coupling problem for subnanometre-thick TMDC waveguides. The patterned PhC structure folds the waveguide mode dispersion, which originally lies below the light line, back to the first Brillouin zone. Consequently, the folded dispersion leads to guided-mode, or Fano, resonances, which are classified as resonant type Wood's anomalies¹⁴. Compared with the true waveguide modes in unpatterned TMDC membranes that are pure bound states without out-of-plane coupling, the guided-mode resonances in TMDC PhC membranes are quasi-bound to the TMDC membranes with only a small portion of light diffracted to the far field ^{15,16}. This enables the probing of the TE waveguide mode via far-field measurements^{14,17} (Supplementary Section 3).

As such, we fabricated atomically thin tungsten disulfide (WS₂) PhC membranes suspended in air, which ensures that the

refractive indices on the top and bottom are inherently the same and enables the waveguide mode at this ångström thickness limit (Supplementary Sections 1-4). Figure 1a exemplifies atomically thick resonant PhCs that consist of square arrays of air holes etched into free-standing WS2 layers with thicknesses that range from h = 2.472 nm (that is, four layers, 4L) down to h = 0.618 nm (that is, a monolayer, 1L)18. In this extreme deep subwavelength limit, the wavelength (λ) to waveguide thickness (h) ratio can reach values >1,000 for visible light ($\lambda \approx 650 \, \text{nm}$). In addition to the characteristic material-dependent WS, excitonic feature, a Fano resonance emerges in the measured far-field spectrum as a new structuredependent spectral feature. This Fano resonance arises because the PhC acts as a second-order grating that mediates the coupling of light into the WS2 PhC guided-mode resonance in the near field (Fig. 1b and Supplementary Section 5), which in turn efficiently couples to the true guided mode in the unpatterned part of WS₂ (Supplementary Section 6).

Waveguiding in suspended WS₂ membranes

The WS, waveguide mode is TE in nature. The electric field is always in-plane polarized perpendicular to the propagation direction (Fig. 1c). Being guided along an ultrathin layer, the mode decays exponentially away from the waveguide, like a typical evanescent wave. By measuring the WS₂ refractive index as a function of the number of layers (Fig. 1d and Supplementary Section 7), we can calculate mode parameters such as the complex effective mode index ($N_{\text{eff}} = n_{\text{eff}} + j\kappa_{\text{eff}}$) where n_{eff} and κ_{eff} are the real and imaginary parts, respectively), propagation length and mode width (Fig. 1c and Supplementary Section 8). Although the mode is confined to an effective width, W_{eff} on the order of the visible wavelength, the energy in the mode is mostly in the air due to the small volume of the subnanometre-thick WS2 layer. This leads to an effective mode index, n_{eff} , of 1.0018 at 660 nm for a monolayer (Fig. 1c). The $n_{\rm eff}$ is only slightly different from the refractive index of air, which makes it extremely challenging to distinguish from the scattering of light into free space. This picture is further complicated because

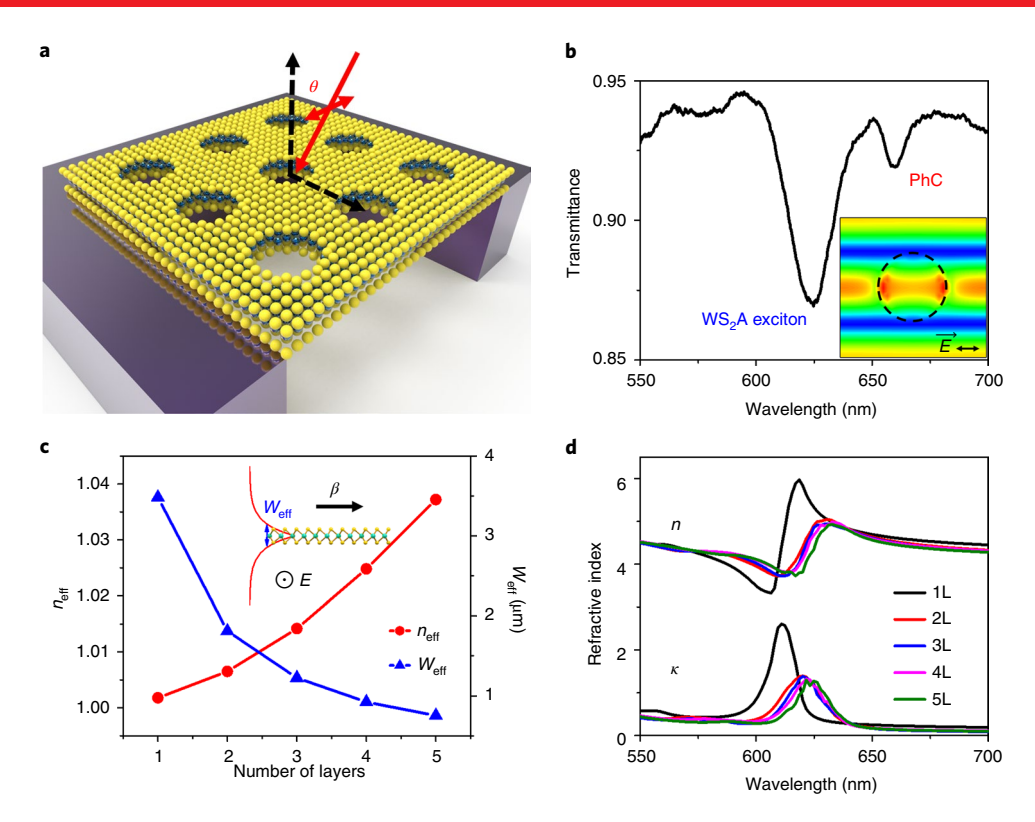


Fig. 1 Atomically thick WS₂ PhC membranes. **a**, A schematic of the monolayer (1L) WS₂ PhC membrane suspended on a silicon frame. The WS₂ PhC membrane consists of a square lattice array of air holes etched into a free-standing WS₂ crystal. The yellow and blue hard spheres represent the S and W atoms, respectively. The black dashed lines and θ indicate the incidence plane and angle, respectively. The illumination is polarized normal to the incidence plane (that is, TE polarized). **b**, The measured transmission spectra for a bilayer (2L) WS₂ PhC membrane with an array period Λ = 660 nm and a hole radius r = 160 nm. Two spectral features as dips are observed in the transmission spectra: that near 620 nm is due to the WS₂ A exciton absorption and that near 660 nm corresponds to the PhC guided-mode resonance. Inset: the calculated electric field profile for the guided-mode resonance in a single unit cell of the 2L WS₂ PhC membrane. The black dashed circle indicates the boundary of the air hole. **c**, The real part (n_{eff}) of the complex effective mode index ($N_{\text{eff}} = n_{\text{eff}} + j\kappa_{\text{eff}}$) and the effective mode width (W_{eff}) for the TE mode versus the unpatterned WS₂ membrane thickness at λ = 660 nm. Inset: schematic of the TE mode with the in-plane electric field E and a propagation constant β in a monolayer WS₂ waveguide. **d**, The measured real (n) and imaginary (κ) parts of the thickness-dependent WS₂ refractive indices.

the mode is only supported if the refractive indices of the media on the top and bottom of WS₂ differ by less than 1% from each other (Supplementary Sections 1 and 2). Another way to see this is by considering that a symmetric dielectric slab waveguide will not have a mode cutoff and hence supports a fundamental mode even at 'zero' thickness (Supplementary Section 1)¹⁹. In our experiments, the symmetric configuration with the WS₂ membrane suspended in air automatically satisfies this crucial requirement.

As $n_{\rm eff}$ approaches 1, the WS₂ waveguide has a significantly stronger mode confinement and, therefore, a larger $n_{\rm eff}$ compared to that of non-excitonic dielectric materials at this ångström thickness limit (Supplementary Section 8). This proves to be critical for the far-field probing of light guiding in our atomically thin WS₂ waveguides. For the guided-mode resonances to be observable in the far field, we rely on the Bragg scattering induced by the periodicity of the PhC that folds the guided modes above the light line 14,20. The Bragg scattering efficiency and consequently the visibility of the PhC guided-mode resonances depend strongly on the refractive index contrast relative to the air holes etched into an otherwise uniform WS₂ membrane suspended in air. This makes the large WS₂ refractive index a crucial parameter to clearly distinguish the light guiding along the atomically thin waveguide in the far field (Supplementary Section 9).

Guided-mode resonances in few-layer WS, PhCs

Figure 2a shows the fabricated free-standing 4L WS₂ PhC membranes (Supplementary Section 10 gives the fabrication details).

We experimentally observed resonant features in the transmission spectra for these WS₂ PhC membranes (Fig. 2c). If the observed resonant features are, indeed, due to the guided-mode resonances that arise from the second-order Bragg condition, we expect the resonant wavelength to depend strongly on the PhC period (Λ). This behaviour is clearly visible in the simulation results shown in Fig. 2b for a 4L WS₂ PhC with different periods for the same hole radius $r = 160 \, \text{nm}$. The period determines the amount of in-plane photon momentum that the PhC provides to scatter normally incident light into the guided-mode resonance in the near field, which in turn changes the WS₂ PhC guided-mode resonance. The simulation data in Fig. 2b show that increasing the WS₂ PhC period causes a redshift in the guided-mode resonance. Our optical measurements (Fig. 2c) for 4L WS₂ PhCs with different periods are in good agreement with the simulations.

Similarly, the guided-mode resonance wavelength can be tuned by changing the incidence angle, which provides another way to probe the guided-mode resonance at different wavelengths¹⁴. This is possible due to the angle-dependent photonic band structure, as shown in Fig. 3b for a 4L WS₂ PhC simulation. In the measured angle-resolved transmission spectra (Fig. 3a), we observed that the resonance wavelength indeed exhibited an angle-dependent behaviour.

To demonstrate the light guiding when the thickness is reduced down to the monolayer limit, we fabricated 2L and 1L WS₂ PhC membranes with the same geometrical parameters as the previous 4L WS₂ PhC membrane and probed the guided-mode resonances

NATURE NANOTECHNOLOGY ARTICLES

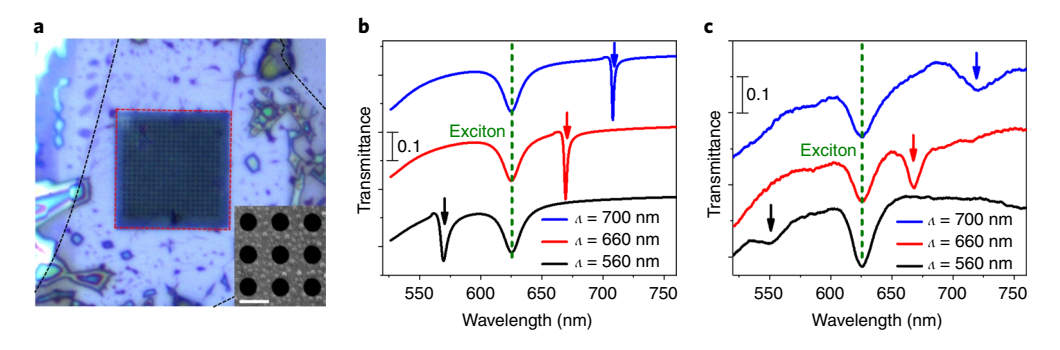


Fig. 2 | Experimental demonstration of WS₂ guided-mode resonances. a, An optical micrograph of a free-standing $4L WS_2 PhC$. The dashed red square indicates the suspended region. The black dashed line indicates the boundary of the $4L WS_2 crystal$. Inset: Scanning electron micrograph of a free-standing $4L WS_2 PhC$ membrane. The bright dispersed dots are the residues due to the hydrogen fluoride step that introduces extra scattering losses. Scale bar, $500 \text{ nm. } \mathbf{b}, \mathbf{c}$, The calculated (**b**) and measured (**c**) transmission spectra for free-standing $4L WS_2 PhC$ membranes with different array periods for the same r = 160 nm. The guided-mode resonance redshifts with increasing PhC period. The vertical arrows mark the guided-mode resonances in **b** and **c**.

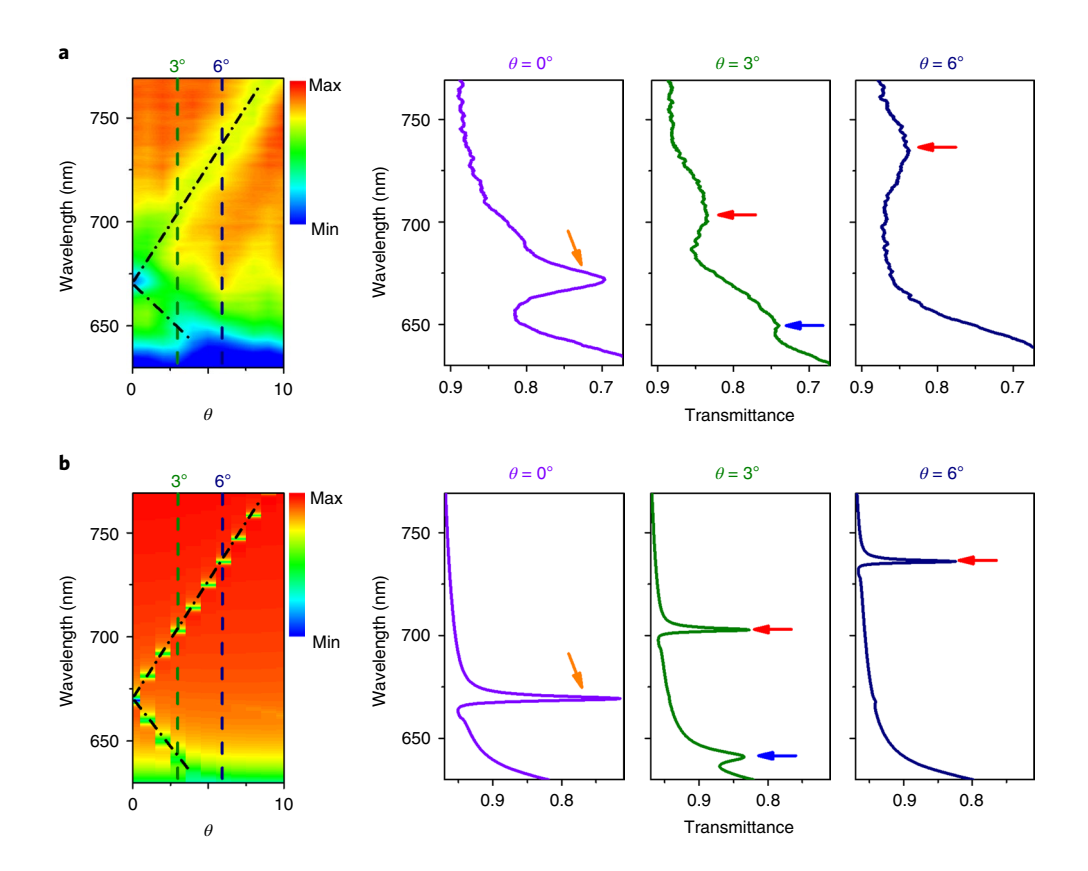


Fig. 3 | The angle dependence of WS₂ guided-mode resonances. a,b, The measured (a) and calculated (b) angle-resolved transmission spectra for TE-polarized illumination. The black dot-dash lines mark the PhC guided-mode resonances, which follow the photonic bands of the WS₂ PhC. The upper branch (that is, the one with a longer wavelength) redshifts with increasing θ, whereas the lower branch blueshifts. The panels on the right show vertical slices at θ = 0°, 3° and 6°. The red and blue arrows denote the upper and lower branches, respectively, of the guided-mode resonances. At the normal incidence (θ =0°), a single guided-mode resonance is observed at 670 nm, which indicates that the far-field illumination couples into the 4L WS₂ guided-mode resonance at λ =670 nm. At an oblique incidence (θ >0°), the guided-mode resonance can be excited at two different wavelengths due to the two non-degenerate photonic bands of the WS₂ away from the Γ point (θ =0°). At θ =3°, two guided-mode resonances at 710 nm and 650 nm are visible in the measured transmission spectrum (a), consistent with the calculations (b). For θ >5°, the shorter wavelength guided-mode resonance disappears due to an increased optical loss in the guided-mode resonance that arises from the crossing over the A exciton absorption peak near 620 nm.

at normal incidence. As can be seen in the transmission spectra plotted in Fig. 4a, when the PhC thickness is reduced from 4L to 2L, the dip in the measured transmission spectrum associated with the guided-mode resonance blueshifts and becomes shallower, which indicates a smaller coupling to the far field. The reduced far-field

coupling is attributed to a decrease in the Bragg scattering efficiency due to a smaller $n_{\rm eff}$ for thinner crystals, which results in a smaller field overlap with the holes (Fig. 1c). With the measured resonance wavelength and linewidth, we can calculate both the real and imaginary parts of $N_{\rm eff}$. The real part of $N_{\rm eff}$ is 1.0006 and

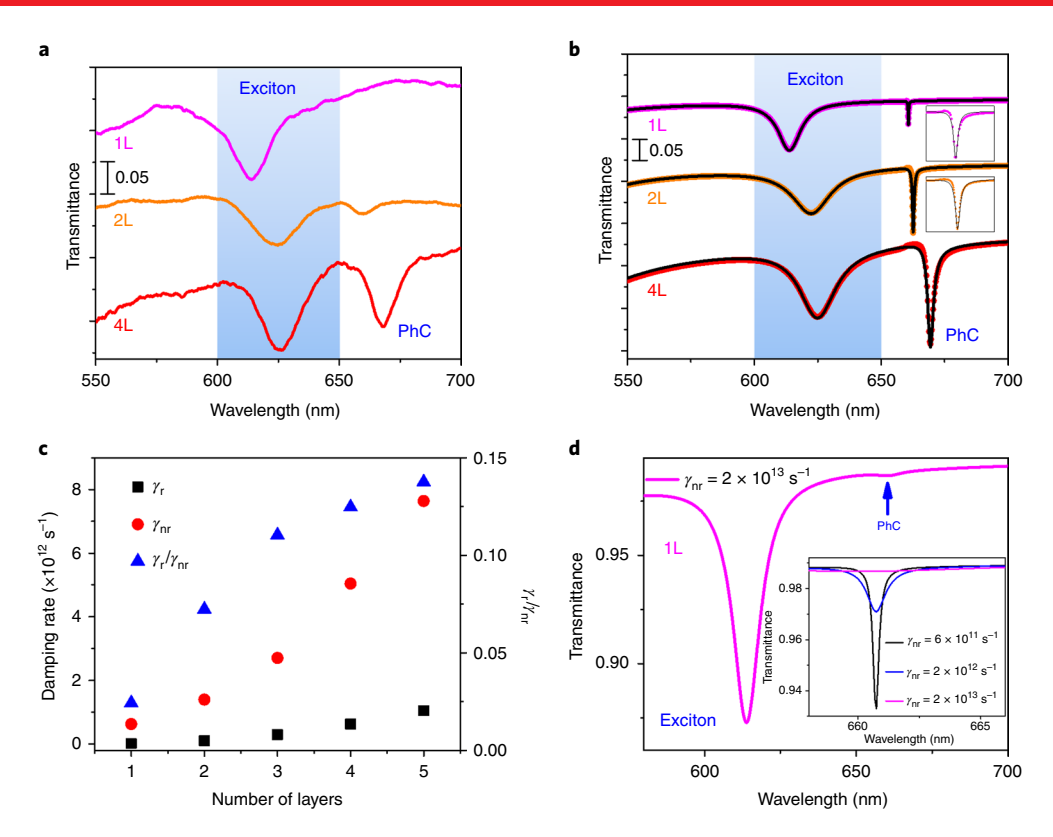


Fig. 4 | The thickness dependence of WS₂ guided-mode resonances. a, The measured transmission spectra for 4L, 2L and 1L WS₂ PhC membranes with Λ = 660 nm and r = 160 nm. The dip associated with the PhC guided-mode resonance becomes shallower when the thickness changes from 4L to 2L, and finally vanishes for 1L WS₂ PhC. **b,** The calculated transmission spectra (dots) for the WS₂ PhC membranes in **a.** The black lines are coupled-mode theory fits based on equation (1). The dip associated with the PhC guided-mode resonance becomes shallower when the thickness changes from 4L to 1L. The insets are enlarged plots of the 1L and 2L PhC guided-mode resonances. **c,** The coupled-mode theory fitting parameters γ_r and γ_{rr} for WS₂ PhC membranes in **b** and the corresponding ratio of γ_{rr}/γ_{rr} **d,** The calculated transmission spectra using equation (1) with the γ_{rr} extracted from the experiment accounting for the fabrication-induced losses for the 1L WS₂ PhC membrane with the same geometry as in **b**. As the γ_{rr} increases in the experiment, γ_{rr}/γ_{rr} decreases to the point that the 1L WS₂ PhC guided-mode resonance becomes invisible, which emulates the experiment. Inset: evolution of the visibility of 1L WS₂ PhC guided-mode resonance with increasing γ_{rr} .

1.0120, respectively, for 2L and 4L WS $_2$ PhC, whereas the imaginary part of $N_{\rm eff}$ is 0.0078 and 0.0100, respectively, for 2L and 4L WS $_2$ PhC (Supplementary Section 3). We also see that the measured resonances are all broader and shallower than those calculated (Fig. 4b). For the monolayer PhC, the guided-mode resonance contrast cannot be distinguished from the fluctuations in transmission intensity in the measurement (Fig. 4a), whereas it is clearly visible in the calculations (Fig. 4b).

To understand these observations, we used the temporal coupled-mode theory to investigate how the guided-mode resonances in the WS₂ PhC membrane depend on different loss mechanisms 14,21 . We found that the transmittance of a WS₂ PhC membrane can be given by:

$$T(\omega) = \frac{(t(\omega - \omega_0) + r\gamma_r)^2 + (t\gamma_{nr})^2}{(\gamma_r + \gamma_{nr})^2 + (\omega - \omega_0)^2}$$
(1)

where ω_0 is the guided-mode resonance frequency, γ_r and γ_{nr} are the damping rates that correspond to the leakage into the far field and the material absorption, respectively, and t and r are the transmission and reflection coefficients of the unpatterned WS₂ membrane, respectively (Supplementary Section 5). The fitting parameters γ_r and γ_{nr} for different WS₂ PhC thicknesses in Fig. 4b are plotted in Fig. 4c. When the WS₂ membrane thickness is reduced from 4L to 1L, $n_{\rm eff}$ decreases and $W_{\rm eff}$ increases, which leads to a reduced material absorption and Bragg scattering efficiency (Supplementary

Section 9). This results in a decrease in both $\gamma_{\rm nr}$ and $\gamma_{\rm r}$. However, $\gamma_{\rm r}$, which determines the efficiency of scattering into the far field and allows us to probe the guided-mode resonance, decreases at a faster rate than $\gamma_{\rm nr}$ does, which leads to a sharp drop in $\gamma_{\rm r}/\gamma_{\rm nr}$ as the thickness decreases (Fig. 4c). For the 1L WS₂ PhC membrane, $\gamma_{\rm r}/\gamma_{\rm nr}\approx 1/40$, which indicates that most of the light is guided in the monolayer and eventually dissipated due to material absorption. A closer examination of equation (1) shows that in the atomic thickness limit away from the WS₂ exciton peak ($t^2\approx 1$ and $t^2\approx 0$), the transmittance $T(\omega_0)\approx 1/(\gamma_{\rm r}/\gamma_{\rm nr}+1)^2$ at the guided-mode resonance frequency ($\omega=\omega_0$) (Supplementary Section 5). Therefore, we can conclude that a smaller $\gamma_{\rm r}/\gamma_{\rm nr}$ leads to a shallower transmittance on resonance (that is, a lower contrast) for the thinner WS₂ PhC membranes. Consequently, the transmission dip associated with the guided-mode resonance becomes shallower as we go from a 4L to a 1L WS₂ PhC membrane.

The same analysis can be used to address guided-mode resonances broader and shallower than those calculated (Fig. 4b). These differences can be readily explained with a larger $\gamma_{\rm nr}$ attributed to the fabrication-related disorder scattering (Fig. 2a and Supplementary Fig. 14) and the finite size of our WS₂ PhCs (Supplementary Section 11). This additional contribution to $\gamma_{\rm nr}$ can account for a larger overall damping rate and reduced transmission contrast $(1-T(\omega_0))$, which leads to the vanishing visibility of the guided-mode resonance for the monolayer case in the experiment (Fig. 4a). We emulate this behaviour in the Fig. 4d inset by plotting the

NATURE NANOTECHNOLOGY ARTICLES

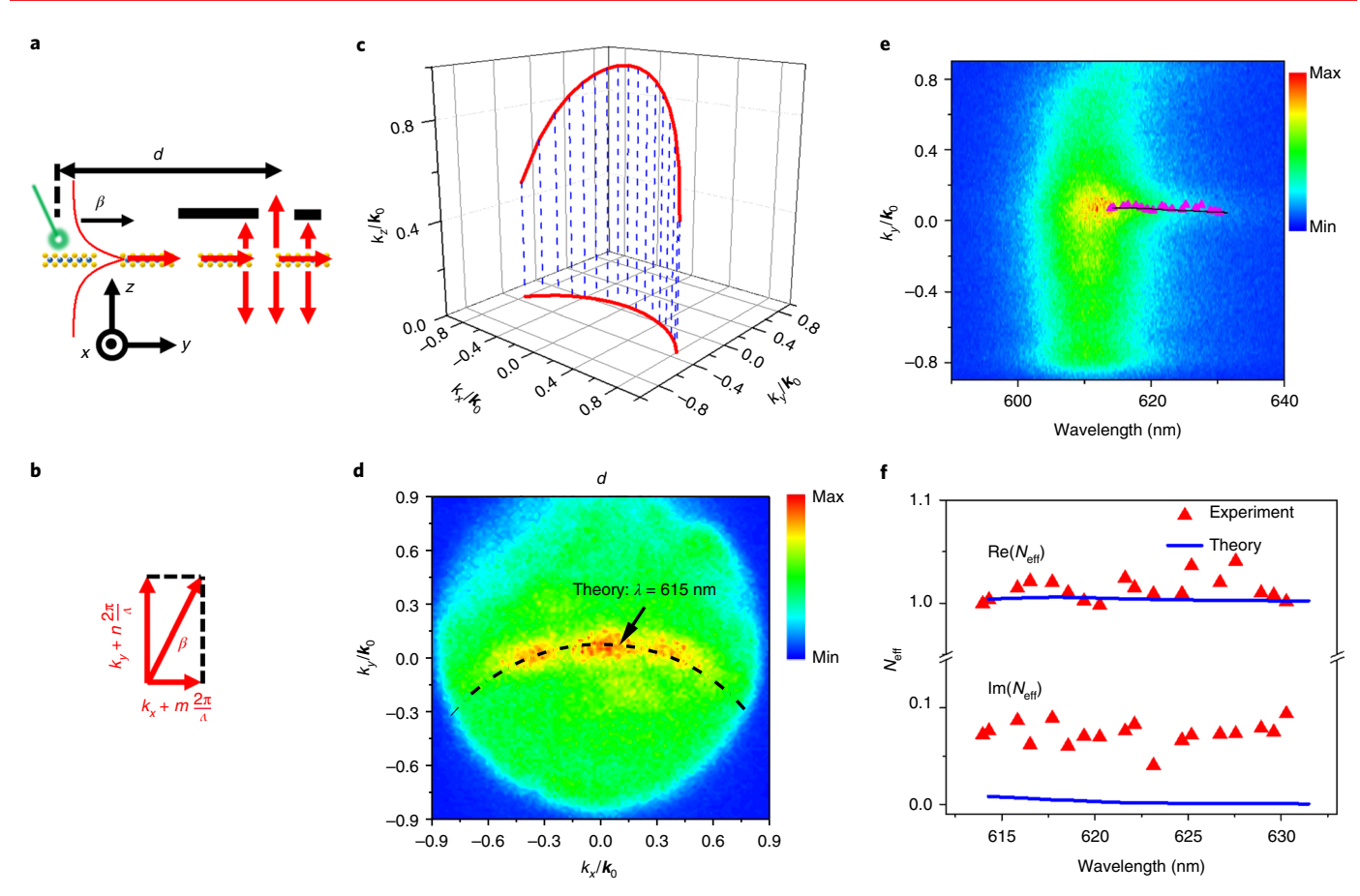


Fig. 5 | Observation of monolayer WS₂ guided-mode resonance. a, The schematic side view (that is, y-z plane) of the 1L WS₂ PhC membrane. A slit was placed at a distance (d) away from the excitation spot as a spatial filter, so that only the light that propagated along the 1L WS₂ PhC and reached the slit position could be detected in the far field. **b**, A schematic for momentum matching in the x-y plane. k_x and k_y are the in-plane components of the output wavevector \mathbf{k}_0 , β is the propagation constant of the guided-mode resonance in the 1L WS₂ PhC membrane and m and n are mode orders. **c**, The calculated output wavevector components k_x , k_y and k_z of 1L WS₂ PhC guided-mode resonance at the exciton emission peak wavelength λ = 615 nm using equation (2) (m = 0, n = 1). **d**, The PL far-field emission patterns of the 1L WS₂ PhC measured 8 μm away from the excitation spot. The black dashed lines are calculated using equation (2) with m = 0 and n = 1. **e**, The angle-resolved PL spectrum for the 1L WS₂ PhC measured 8 μm away from the excitation spot. The pink triangles and the black line are the measured and calculated peaks of emission angles, respectively. **f**, The measured complex effective mode index (N_{eff}) of 1L WS₂ guided-mode resonance in the wavelength range 614-631 nm. Owing to the fabrication imperfections, the imaginary part of N_{eff} is larger than the theoretical value.

evolution of the calculated 1L WS₂ PhC transmittance near the guided-mode resonance for increasing values of γ_{nr} . To further corroborate our analysis, we calculated the transmission spectra using the extracted γ_{nr} from the experimental data (Fig. 4a,d and Supplementary Sections 12 and 13). Using equation (1), we extracted a value of $2\times10^{13}\,\mathrm{s^{-1}}$ for γ_{nr} . The calculated transmission spectrum for 1L WS₂ PhC agrees well with the measured one (Fig. 4a,d). This indicates that the imperfections in fabrication significantly reduce the visibility of the guided-mode resonance and cause it to be indistinguishable within the intensity noise of the transmission measurements for the monolayer case (Fig. 4a).

Guided-mode resonances in monolayer WS, PhCs

To demonstrate experimentally the 1L WS₂ PhC guided-mode resonance, we resorted to an alternative approach based on PL to eliminate the directly transmitted light background and enhance the signal-to-background ratio for the guided-mode resonance. To this end, we detected the PL light guided to a distance from the excitation spot, which completely eliminates the transmitted background (Fig. 5a,b). We used a green laser (λ =532 nm) to excite the 2D exciton PL emission, which in turn coupled into the guided-mode resonance in the 1L WS₂ PhC (Fig. 5a,b). The guided light with an

in-plane propagation constant ($\beta = n_{\rm eff} k_0$) was modulated by the PhC structure with a grating period Λ and diffracted into the free space. As shown in Fig. 5b, the momentum matching condition between the guided-mode resonance and the in-plane components (k_x and k_y) of the free-space wavevector (\mathbf{k}_0) requires (Supplementary Section 3):

$$(n_{\text{eff}})^2 = \left(\frac{k_x}{\mathbf{k}_0} + m \frac{2\pi}{\Lambda \mathbf{k}_0}\right)^2 + \left(\frac{k_y}{\mathbf{k}_0} + n \frac{2\pi}{\Lambda \mathbf{k}_0}\right)^2, m, n = 0, 1, 2, \dots$$
(2)

Therefore, the diffracted light forms an arc in the momentum space that is centred at $\left(-m\frac{2\pi}{\Lambda k_0},-n\frac{2\pi}{\Lambda k_0}\right)$ with a radius of $n_{\rm eff}$ (Fig. 5c). In the experiment, we used, as a spatial filter, a slit positioned 8 µm away from the excitation spot to allow only the light scattered from a specific region to be detected in the far field (Fig. 5a,b). We then used an objective to collect the diffracted light and project the Fourier plane onto a camera. As can be seen in Fig. 5d, the guided PL is diffracted by the 1L WS₂ PhC and forms a bright arc in the momentum space. Calculation reveals that the observed bright arc agrees well with the (0,1) order diffraction

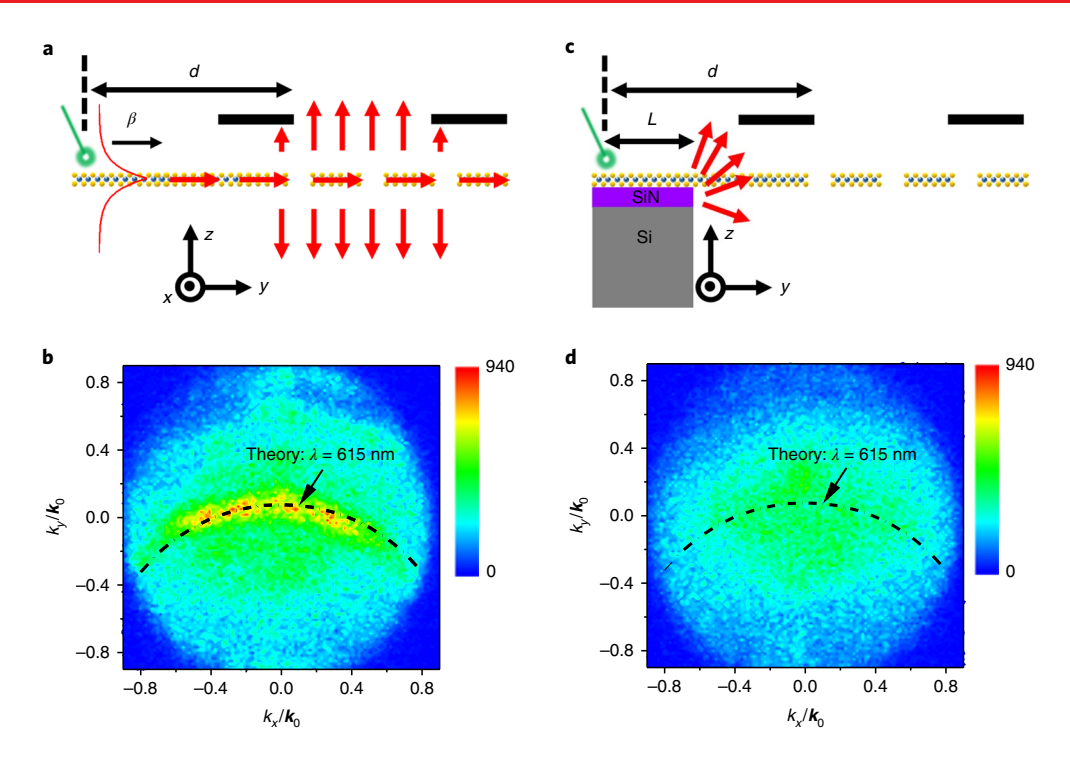


Fig. 6 | Coupling of the WS₂ waveguide mode to guided-mode resonance. **a**, A schematic side view (that is, y-z plane) of coupling of the waveguide mode in an unpatterned 1L WS₂ to the guided-mode resonance of a 1L WS₂ PhC membrane. A green laser (λ = 532 nm) was used to excite the PL emission, which coupled to the waveguide mode in the unpatterned WS₂ region and then coupled to the guided-mode resonance in the PhC region with Λ = 660 nm and r = 160 nm. The guided light slowly leaked out from PhC region and radiated into free space (free-space wavevector \mathbf{k}_0). A slit was placed at a distance (d = 4.5 μ m) away from the excitation spot as a spatial filter, so that only the light that propagated along the unpatterned WS₂ and reached the slit position could be detected in the far field. **b**, The PL far-field emission patterns measured with the scheme shown in **a**. The black dashed lines are calculated using equation (2) with m = 0 and n = 1. **c**, Schematic side view (that is, y-z plane) of the control experiment of **a**. The unpatterned WS₂ was partially placed on the substrate (L = 3 μ m), and the PL emission was excited from WS₂ on the substrate. As no waveguide mode can be supported in the WS₂ on the substrate, the PL can only couple to the guided-mode resonance in the PhC region by free-space scattering. **d**, The PL far-field emission patterns measured with the scheme shown in **c**. The black dashed lines are calculated using equation (2) with m = 0 and n = 1.

mode (that is, m = 0, n = 1) of the 1L WS₂ PhC, which confirms the existence of a guided-mode resonance in the 1L WS₂ PhC membrane (Supplementary Section 14).

To determine the complex mode index in the 1L WS₂ PhC membrane, we measured the angle-resolved PL spectra with the scheme in Fig. 5a. Light emitted by excitons in 1L WS₂ was coupled to the guided-mode resonances and redistributed into specific angles (Fig. 5e). By taking vertical line scans in Fig. 5e and fitting the angular emission profiles, we can obtain the emission angles and angular line widths for each wavelength, from which we can determine the complex mode index (Supplementary Section 15). Figure 5f shows both the measured and calculated complex mode indices ($N_{\rm eff}$) in the wavelength range 614–631 nm. It can be seen that the real part of $N_{\rm eff}$ is close to but always slightly larger than 1, which indicates a weakly confined optical mode profile. However, owing to the induced fabrication losses, the measured imaginary part of $N_{\rm eff}$ (~10⁻²) is much larger than the calculated value (~10⁻³–10⁻⁴).

Demonstration of waveguide mode in monolayer WS₂

As a quasi-guided mode, the guided-mode resonance in atomically thin WS₂ PhC membranes can not only guide light, but also can be employed as a second-order grating coupler as typically used in the integrated photonics community to couple the waveguide mode in the near field to the far field²². To this end, we partially patterned a suspended 1L WS₂ with PhC structures (Fig. 6a). The unpatterned region supported a true TE waveguide mode and the PhC region supported a guided-mode resonance (that is, quasi-guided mode). We used a 532 nm laser to irradiate the unpatterned region,

in which a true TE waveguide mode was supported. The excited PL could couple to the TE waveguide mode and propagate along the WS_2 for $4.5\,\mu m$. When the guided PL reached the PhC region acting as an outcoupler, which was patterned on one side of the WS_2 membrane, the guided PL supported by the true TE waveguide mode could efficiently couple to the quasi-guided mode with a small diffraction loss supported by the WS_2 PhC membrane. Consequently, the PL guided by the TE waveguide mode, which is a bound state with far-field radiation prohibited in the unpatterned WS_2 membrane, was now coupled to the far field via the guided-mode resonance of the PhC coupler, which led to a PL arc, as shown in Fig. 6b (Supplementary Section 16).

To determine unambiguously that the observed PL arc is due to the coupling of a true waveguide mode to a guided-mode resonance, we have to rule out the possibility of free-space scattering, which may couple the excited PL to the guided-mode resonance directly through free-space propagation. With this in mind, we performed a control experiment in which we excited the PL from the WS₂ on the substrate where no waveguide mode was supported and measured the far-field radiation from the PhC region in the same sample (Fig. 6c). The excited PL in the control experiment can only couple to the guided-mode resonance via free-space scattering, which is expected to be less efficient. Although the overall PL intensity, the distance between the excitation spot and the slit, and slit size for these two experiments were all the same, we did not observe a PL arc in the far-field image (Fig. 6d), which confirms that the strong PL arc in Fig. 6c results from the efficient coupling of the true waveguide mode to the guided-mode resonance (Supplementary Section 16).

NATURE NANOTECHNOLOGY ARTICLES

Conclusions

In conclusion, we have experimentally demonstrated the guiding and coupling of visible light at the ångström thickness limit of PhC membranes based on atomically thin WS₂ crystals. Our approach is based on probing on the far field the TE-guided mode via guided-mode resonances of an atomically thin WS₂ PhC. The light coupling, guiding and resonances at the ångström thickness limit have potential applications in spectral filters, beam splitters, beam shaping, non-linear optics, optomechanics and sensors (Supplementary Section 17). Furthermore, this work can be scaled up to substrate-based symmetric configurations by employing the transfer of wafer-scale high-quality monolayers, which have already been realized by chemical vapour deposition and sputtering methods^{23–25} (Supplementary Section 4).

Data and materials availability

The data that support the plots within this paper and other findings of this study are available from the corresponding author upon reasonable request.

Online content

Any methods, additional references, Nature Research reporting summaries, source data, statements of code and data availability and associated accession codes are available at https://doi.org/10.1038/s41565-019-0519-6.

Received: 13 March 2019; Accepted: 2 July 2019; Published online: 12 August 2019

References

- Ye, Z. et al. Probing excitonic dark states in single-layer tungsten disulphide. Nature 513, 214–218 (2014).
- Ramasubramaniam, A. Large excitonic effects in monolayers of molybdenum and tungsten dichalcogenides. Phys. Rev. B 86, 115409 (2012).
- Mak, K. F. & Shan, J. Photonics and optoelectronics of 2D semiconductor transition metal dichalcogenides. *Nat. Photon.* 10, 216–226 (2016).
- 4. Ye, Y. et al. Monolayer excitonic laser. Nat. Photon. 9, 733-737 (2015).
- Splendiani, A. et al. Emerging photoluminescence in monolayer MoS₂. Nano Lett. 10, 1271–1275 (2010).
- Mak, K. F., Lee, C., Hone, J., Shan, J. & Heinz, T. F. Atomically thin MoS₂: a new direct-gap semiconductor. *Phys. Rev. Lett.* 105, 136805 (2010).
- Tongay, S. et al. Defects activated photoluminescence in two-dimensional semiconductors: interplay between bound, charged, and free excitons. Sci. Rep. 3, 2657 (2013).
- Malard, M., Alencar, T. V., Barboza, A. P. M., Mak, K. F. & de Paula, A. M. Observation of intense second harmonic generation from MoS₂ atomic crystals. *Phys. Rev. B* 87, 201401(R) (2013).
- Li, Y. et al. Probing symmetry properties of few-layer MoS₂ and h-BN by optical second-harmonic generation. *Nano Lett.* 13, 3329–3333 (2013).
- Yi, F. et al. Optomechanical enhancement of doubly resonant 2D optical nonlinearity. Nano Lett. 16, 1631–1636 (2016).
- 11. Zhang, X. et al. Unidirectional doubly enhanced MoS_2 emission via photonic Fano resonances. *Nano Lett.* 17, 6715–6720 (2017).

- Zhang, X. et al. Dynamic photochemical and optoelectronic control of photonic Fano resonances via monolayer MoS, trions. Nano Lett. 18, 957–963 (2018).
- Khurgin, J. B. Two-dimensional exciton-polariton—light guiding by transition metal dichalcogenide monolayers. Optica 2, 740 (2015).
- 14. Fan, S. & Joannopoulos, J. D. Analysis of guided resonances in photonic crystal slabs. *Phys. Rev. B* **65**, 235112 (2002).
- García de Abajo, F. J. Colloquium: light scattering by particle and hole arrays. Rev. Mod. Phys. 79, 1267–1290 (2007).
- Gomez-Medina, R., Laroche, M. & Saenz, J. J. Extraordinary optical reflection from sub-wavelength cylinder arrays. Opt. Express 14, 3730–3737 (2006).
- Wang, S. S. & Magnusson, R. Theory and applications of guided-mode resonance filters. Appl Opt. 32, 2606–2613 (1993).
- Li, Y. et al. Measurement of the optical dielectric function of monolayer transition-metal dichalcogenides: MoS₂, MoSe₂, WS₂, and WSe₂. Phys. Rev. B 90, 205422 (2014).
- 19. Hunsperger R. G. Integrated Optics: Theory and Technology (Springer, 2009).
- Crozier, K. B. et al. Air-bridged photonic crystal slabs at visible and near-infrared wavelengths. *Phys. Rev. B* 73, 115126 (2006).
- Fan, S., Suh, W. & Joannopoulos, J. D. Temporal coupled-mode theory for the Fano resonance in optical resonators. J. Opt. Soc. Am. A 20, 569–572 (2003).
- Taillaert, D. et al. An out-of-plane grating coupler for efficient butt-coupling between compact planar waveguides and single-mode fibers. *IEEE J. Quantum Electron* 38, 949–955 (2002).
- 23. Yang, J. et al. Wafer-scale synthesis of thickness-controllable MoS₂ films via solution-processing using a dimethylformamide/n-butylamine/2-aminoethanol solvent system. Nanoscale 7, 9311–9319 (2015).
- Yu, H. et al. Wafer-scale growth and transfer of highly-oriented monolayer MoS, continuous films. ACS Nano 11, 12001–12007 (2017).
- Tao, J. et al. Growth of wafer-scale MoS₂ monolayer by magnetron sputtering. Nanoscale 7, 2497–2503 (2015).

Acknowledgements

This work was partially supported by the National Science Foundation (NSF) under the NSF 2-DARE Program (EFMA-1542879 and EFMA-1542863) and DMR-1709996. We thank R. Agarwal and R. Bratschitsch for useful discussions during the early stages of this work.

Author contributions

X.Z. and E.C. conceived the idea. X.Z. and C.D.-E. fabricated the devices. J.G., A.L.B. and V.M.M. provided the WS₂ crystals and their reflection spectra. X.Z. performed theoretical modelling. X.Z. and C.D.-E. performed optical measurements and data analysis. C.D.-E. performed the atomic force microscopy measurements. J.K provided the theoretical support for the original 2D waveguiding analysis. E.C. supervised the study. All the authors contributed to the writing of the paper.

Competing interests

The authors declare no competing interests.

Additional information

 $\label{eq:supplementary information} \textbf{Supplementary information} \ is available for this paper at \ https://doi.org/10.1038/s41565-019-0519-6.$

Reprints and permissions information is available at www.nature.com/reprints.

Correspondence and requests for materials should be addressed to E.C.

Publisher's note: Springer Nature remains neutral with regard to jurisdictional claims in published maps and institutional affiliations.

© The Author(s), under exclusive licence to Springer Nature Limited 2019

Methods

Fabrication. We first fabricated a PhC by direct focused ion beam lithography with the desired period and hole size in a 20 nm thick free-standing silicon nitride (SiN) membrane with the lateral dimensions of $20\,\mu\text{m}\times20\,\mu\text{m}$. Next, we transferred a mechanically exfoliated WS₂ crystal onto the SiN PhC. Then, by using the SiN PhC as an etch mask, the PhC pattern was etched into the WS₂ crystal by reactive-ion etching. Finally, the WS₂ PhC membrane was suspended in air by removing the SiN sacrificial layer through hydrofluoric acid (HF) vapour etching. The HF vapour can react with SiN, but has no effect on the optical properties of WS₂, which allowed us to safely remove the SiN layer without destroying the WS₂ crystals. PL measurements taken postprocessing further confirmed that the WS₂ crystals were, indeed, preserved

after HF vapour release. More details of the fabrication process are provided in Supplementary Section 10.

Optical characterization. To measure the transmission spectrum of the PhC membranes, the collimated white light emitted by a stabilized broadband tungstenhalogen light source was polarized and then illuminated on the sample in the normal direction. The transmitted light was collected by a long working distance $\times 50$ objective (NA = 0.42) and measured by a spectrometer equipped with a cooled charge-coupled device camera. In front of the spectrometer, an adjustable 2D slit was used as a spatial filter to select a $2\times 2\,\mu\text{m}^2$ area of the sample plane. For the angle-resolved transmission spectrum measurement, the sample was rotated as the incident beam was fixed to tune the incident angle.